Preprint typeset using LaTeX style emulateapj v. 12/16/11

arXiv:2206.11438v3 [astro-ph.HE] 30 Dec 2022

THERMAL AND NONTHERMAL EMISSION FROM A PECULIAR LONG-DURATION GRB 211211A

Xue-Zhao Chang[1], Hou-Jun Lü[1], Xing Yang[1], Jia-Ming Chen[2], and En-Wei Liang[1]

ABSTRACT

Long-duration GRB 211211A that lacks a supernova emission even down to very stringent limits at such a low redshift $z = 0.076$ and is associated with kilonova emission, suggests that its physical origin is from a binary compact star merger. By reanalyzing its data observed with the Gamma-Ray Burst Monitor on board the Fermi mission, we find that both time-integrated and time-resolved spectra can be fitted well by using a 2SBPL plus blackbody (2SBPL+BB) model in the prompt emission. The bulk Lorentz factors ($\Gamma_{\rm ph}$) of the outflow can be inferred by invoking the observed thermal emission at the photosphere radius within a pure fireball model, and we find out that the temporal evolution of $\Gamma_{\rm ph}$ seems to be tracking with the light curve. The derived values of $\Gamma_{\rm ph}$ are also consistent with the $\Gamma_{\rm ph}$-$L_{\gamma,\rm iso}/E_{\gamma,\rm iso}$ correlations that had been found in other bursts. Moreover, we also calculate the magnetization factor σ_0 in the central engine and $\sigma_{\rm ph}$ at the photosphere radius within the framework of a hybrid jet model, and find that the values of both $1+\sigma_0$ and $1+\sigma_{\rm ph}$ are larger than 1 for different time slices. It suggests that at least the Poynting-flux component is indeed existent in the outflow. If this is the case, one possible physical interpretation of thermal and nonthermal emissions in GRB 211211A is from the contributions of both $\nu\bar{\nu}$ annihilation and the Blandford-Znajek mechanisms in the relativistic jet when a stellar mass black hole resides in the central engine.

Subject headings: Gamma-ray burst: general

1. INTRODUCTION

The field that studies of gamma-ray bursts (GRBs) has made a great progress in both observations and theories (see Kumar & Zhang 2015, for a review). In general, GRBs are thought to be from a catastrophic event (such as massive star core collapse or the merger of two compact stars) to release its gravitational energy that is converted in the form of thermal energy, and a central engine (black hole or neutron star) is formed after the catastrophic event (Eichler et al. 1989; Usov 1992; Thompson 1994; Dai & Lu 1998a,b; Popham et al. 1999; Narayan et al. 2001; Zhang & Mészáros 2001; Lei et al. 2009; Metzger et al. 2011; Bucciantini et al. 2012; Lü & Zhang 2014; Berger 2014; Lü et al. 2015). The fireball model is the most popular one to interpret both γ-ray emission and broadband afterglow emission of GRB phenomena (Mészáros & Rees 1997; Sari et al. 1998; Mészáros 2002; Zhang & Mészáros 2004; Zhang et al. 2016). The observed prompt emission can be explained by the photosphere with a quasi-thermal spectrum (Paczynski 1986; Goodman 1986), or internal shocks with a nonthermal electromagnetic radiation (Rees & Meszaros 1994), or dissipation of the magnetic energy with a nonthermal spectrum at a large radius (Zhang & Yan 2011).

Within the above scenario, the photons that are produced in the thermalized outflow can escape near the photospheric radius when the optical depth is close to 1, and a purely quasi-thermal component should be observed in the prompt emission of a GRB, such as GRB 090902B (Abdo et al. 2009; Ryde et al. 2010; Zhang et al. 2011). On the contrary, if the outflow is Poynting-flux dominated, it should produce a purely nonthermal emission, such as GRB 080916C (Zhang & Pe'er 2009). In general, the dissipated radius of the photospheric and internal shock cannot be distinguished very well, and the observed spectrum of GRB prompt emission should be the superposition of thermal and nonthermal components (Ryde 2005; Gao & Zhang 2015). Such evidence of thermal and nonthermal emission is already found in several solid cases, e.g., GRB 100724B (Guiriec et al. 2011); GRB 110721A (Axelsson et al. 2012); GRB 120323A (Guiriec et al. 2013); GBR 160625B (Lü et al. 2017); GRB 081221 (Hou et al. 2018).

Most recently, a peculiar and nearby long-duration GRB 211211A that triggered the Fermi Gamma-Ray Burst Monitor (GBM; Mangan et al. 2021), Swift Burst Alert Telescope (BAT; D'Ai et al. 2021), as well as Insight-HXMT (Zhang et al. 2021), is very excited for attention with redshift z=0.076. The light curve of prompt emission is composed of an initial hard-main emission (with a duration ~ 13 s) followed by a series of soft gamma-ray extended emission (EE) with a duration ~ 55 s, and the structure of the light curve is similar to the particularly interesting case GRB 060614(Yang et al. 2022; Xiao et al. 2022) and GRB 211227A (Lü et al. 2022). More interestingly, no associated supernova signature is detected for GRB 211211A, even down to very stringent limits at such a low redshift, but associated with kilonova is observed by several optical telescopes (Rastinejad et al. 2022). That observed evidence suggests that GRB 211211A is originated from a binary compact star merger (Rastinejad et al. 2022; Yang et al. 2022; Xiao et al. 2022; Gompertz et al. 2022). However, how to produce such long-duration emission within the compact star merger scenario remains an open question. Gao et al. (2022) proposed that the black hole central engine surrounded by a strong magnetic flux can

[1] Guangxi Key Laboratory for Relativistic Astrophysics, School of Physical Science and Technology, Guangxi University, Nanning 530004, China; lhj@gxu.edu.cn
[2] School of Physics and Astronomy, Yunnan University, Kunming 650500, China

well interpret the behavior of long-duration emission of GRB 211211A. Gompertz et al. (2022) found that the spectrum can be fitted well with a double smoothly broken power-law model SBPL, which is interpreted as synchrotron emission, including both characteristic synchrotron frequency (ν_m) and the cooling frequency (ν_c). So that identifying the composition of the jet in such a binary system will play an important role in understanding the physical process and mechanism (Zhang et al. 2011; Kumar & Zhang 2015; Zhang 2018).

In this paper, by analyzing the data observed with the GBM on board the Fermi mission, we find that a blackbody emission with a nonthermal component 2SBPL function can be fitted well to the spectra in the prompt emission of GRB 211211A, especially in the initial hard-main emission phase. It means that the thermal component should be indeed existent, and it is different from previous studies that claimed the single nonthermal component is dominated in the prompt emission phase (Yang et al. 2022; Xiao et al. 2022). The data analysis and spectral fitting are presented in §2. In §3, we derive the Lorentz factor of the jet, its photospheric radius, magnetization σ_0, and the dimensionless entropy η based on the observed thermal and nonthermal emissions of GRB 211211A. The conclusions are drawn in §4 with some additional discussion. Throughout the paper, a concordant cosmology with parameters $H_0 = 70$ km s^{-1} Mpc^{-1}, $\Omega_M = 0.30$, and $\Omega_\Lambda = 0.70$ is adopted.

2. FERMI/GBM DATA ANALYSIS

2.1. *Light curve and spectral fits*

GRB 211211A triggered the Fermi/GBM at 13:09:59.651 UT on 2021 December 11 (Mangan et al. 2021). This GRB was also detected by Swift/BAT (D'Ai et al. 2021) and Insight-HXMT (Zhang et al. 2021). We downloaded the corresponding time-tagged-event (TTE) data of GRB 211211A from the public science support center at the official Fermi website[3]. The GBM has 12 sodium iodide (NaI) detectors covering an energy range from 8 keV to 1 MeV, and two bismuth germanate (BGO) scintillation detectors sensitive to higher energies between 200 keV and 40 MeV (Meegan et al. 2009). We select the brightest NaI and BGO detectors for the analyses, namely n2, na and b0. For more details of data reduction of the light curve, please refer to Lü et al. (2017) and Zhang et al. (2018).

We extract the light curves with a 128 ms time bin (Figure 1) by running *gtbin*. The light curve shows a complex structure with a total duration of about T_{90} ~43 s, an initially main emission (with a duration ~ 13 s) followed by a series of soft gamma-ray extended emission with a duration ~ 55 s (also see Yang et al. 2022).

Both time-integrated and time-resolved spectra of this source are extracted from the TTE data. The background spectrum from the GBM data is extracted from the continuous spectroscopy (CSPEC) format data with two time intervals before and after the prompt emission phase and are modeled with a polynomial function. We perform the spectral fit with the multimission maximum likelihood framework package (Vianello et al. 2017), which adopts the Markov Chain Monte Carlo (MCMC) technique to perform time-resolved spectral fitting. Also, we evaluate the goodness of our fits with the maximum likelihood based statistics, the so-called PGSTAT. Yang et al. (2022) invoked a cutoff power-law model to do the spectral fitting in both the time-averaged and time-resolved spectra of GRB 211211A (also see Gompertz et al. 2022). In our analysis, several spectral models can be selected to test the spectral fitting of the burst, such as cutoff power-law (CPL), Band function (Band), a smoothly broken power-law model (SBPL), a double smoothly broken power-law model (2SBPL) and blackbody (BB), as well as combinations of any two models. The Band function (Band et al. 1993) and blackbody function, and CPL models are written as follows:

$$N_{\rm Band}(E) = A \begin{cases} (\frac{E}{100\ \rm keV})^{\alpha} \exp\left[-\frac{(\alpha+2)E}{E_p}\right], E < E_c, \\ (\frac{E}{100\ \rm keV})^{\beta} \exp(\beta-\alpha)(\frac{E_c}{100\ \rm keV})^{\alpha-\beta}, E \geq E_c \end{cases} \quad (1)$$

where A is the normalization of the spectrum, α and β are the low and high-energy photon spectral indices, respectively,and $E_p = (2+\alpha)E_c$ is the peak energy;

$$N_{\rm BB}(E) = A(t)\frac{E^2}{\exp[E/kT]-1} \quad (2)$$

where k and T are Boltzmann constant and temperature, respectively;

$$N_{\rm CPL}(E) = A \cdot E^{-\alpha} \exp(-\frac{\rm E}{\rm E_p}). \quad (3)$$

The SBPL function (Ravasio et al. 2018) function is defined as follows:

$$N_{\rm SBPL}(E) = A\left(\frac{E}{100\ \rm keV}\right)^{b} 10^{(a-a_{\rm piv})} \quad (4)$$

where $a = m\Lambda \ln\left(\frac{e^q+e^{-q}}{2}\right)$, $a_{\rm piv} = m\Lambda \ln\left(\frac{e^{q_{\rm piv}}+e^{-q_{\rm piv}}}{2}\right)$, $q = \frac{\log(E/E_b)}{\Lambda}$, $q_{\rm piv} = \frac{\log(100\ \rm keV/E_b)}{\Lambda}$, $m = \frac{\beta-\alpha}{2}$, $b = \frac{\alpha+\beta}{2}$. Here, α, β and E_b are the lower power-law index, upper power-law index, and a break energy, respectively; Λ is the break scale, which is fixed at 0.3.

The 2SBPL function (Kaneko et al. 2006) function is defined as follows:

$$N_{\rm 2SBPL} = AE_{\rm b}^{\alpha_1}[f_1(E) + f2(E)]^{-\frac{1}{n_2}} \quad (5)$$

where$f_1(E) = [(\frac{E}{E_{\rm b}})^{-\alpha_1 n_1} + (\frac{E}{E_{\rm b}})^{-\alpha_2 n_2}]^{n_2/n_1}$, $f_2(E) = (\frac{E}{E_{\rm j}})^{-\beta n_2}[(\frac{E_{\rm j}}{E_{\rm b}})^{-\alpha_1 n_1} + (\frac{E_{\rm j}}{E_{\rm b}})^{-\alpha_2 n_2}]^{n_2/n_1}$, and $E_{\rm j} = E_{\rm pk} \cdot \left(-\frac{\alpha_2+2}{\beta+2}\right)^{\frac{1}{(\beta-\alpha_2)n_2}}$; α_1 and α_2 are the photon index below and above the break energy, respectively. E_b and E_{pk} are the break energy and peak energy, respectively; β is the high-energy photon index above the peak energy; n_1 (for the break) and n_2 (for the peak) are the smoothness parameters. In this work, we fix the $n_1 = 5.38$ and $n_2 = 2.69$, respectively (Ravasio et al. 2018).

In order to test which model is the best fit with the data, we compare the goodness of the fits by invoking the Bayesian information criteria (BIC)[4]. For the specific

[3] https://heasarc.gsfc.nasa.gov/FTP/fermi/data/gbm/daily/

[4] BIC is a criterion to evaluate the best model fit among a fi-

definition of the goodness of data fitting by the empirical model, please refer to Li (2019). We find that the 2SBPL+BB model is the best one to adequately describe the observed data, and it means that the thermal emission component in GRB 211211A is a significant presence (see Table 1). The spectral fitting result of the time-integrated spectra is shown in Figure 2. Moreover, we find that the photon indices of the time-integrated spectra are $\alpha_1 = -0.6$ and $\alpha_2 = -1.62$, respectively. These values are consistent with the results in Gompertz et al. (2022), and it suggests that the nonthermal component may be originated from the synchrotron emission in the fast regime.

We also extract time-resolved spectral analyses of GRB 211211A between $T_0 + 0.5$ and $T_0 + 70$. We divide the time interval into 31 slices, and fit those slices by invoking 2SBPL and 2SBPL+BB models. The fitting results are shown in Table 2. Figure 1 shows the evolution of ΔBIC, which is defined as $\Delta\mathrm{BIC} = \mathrm{BIC}_{\mathrm{2SBPL}} - \mathrm{BIC}_{\mathrm{2SBPL+BB}}$. We find that the ΔBIC of all time slices is larger than zero, especially, the ΔBIC at the peak of light curve in both the main emission and extended emission is much larger than 10. Even during the late period of the extended emission phase, the ΔBIC of most time slices remains in the range of [6-10]. By comparing the BIC of 2SBPL and 2SBPL+BB models, we find that it is strong to support the 2SBPL+BB model, which is better than the 2SBPL model to describe the observed data during the time-resolved spectra of GRB 211211A. In other words, the thermal emission component in GRB 211211A remains a significant presence in the time-resolved spectrum. By adopting $z = 0.076$ of GRB 211211A, the total isotropic-equivalent energy ($E_{\gamma,\mathrm{iso}}$) and luminosity ($L_{\gamma,\mathrm{iso}}$) can be as high as 7.6×10^{51} erg and 1.9×10^{51} erg s^{-1}, respectively.

2.2. *Fitting results*

In order to test the behavior of temporal evolution of main parameters for thermal and nonthermal emissions, we present the temporal evolution of E_b, E_{pk}, kT, the flux of BB emission (F_{BB}), and the ratio of F_{BB} and total observed flux (F_{obs}) in Figure 3. By comparing the E_b and E_{pk} evolution of both 2SBPL and 2SBPL+BB models, we find that the E_{b} and E_{pk} evolution of 2SBPL+BB model are similar to that of the 2SBPL model, and the behavior of its evolution seems to be tracking with pulses of the light curve. The temperature (kT) and the flux (F_{BB}) of BB emission also exhibits the tracking behavior with its pulses. The F_{BB} can reach to as high as 8.16×10^{-6} erg cm^{-2} s^{-1}. We also calculate the total observed flux, which includes both thermal and nonthermal emission and find that the fraction of thermal emission flux ($F_{\mathrm{BB}}/F_{\mathrm{obs}}$) can reach as high as ~ 0.2. The significant thermal component in the prompt emission is also independent to support the BB emission, which should indeed be presented.

nite set of models, and the lowest BIC of a model is preferred (Neath & Cavanaugh 2012). The definition of BIC can be written as: $BIC = -2\mathrm{lnL} + \mathrm{k} \cdot \mathrm{ln(n)}$, where k is the number of model parameters, n is the number of data points, and L is the maximum value of the likelihood function of the estimated model. (1) if $0 < \Delta BIC < 2$, the evidence against the model with higher BIC is not worth more than a bare mention; (2) if $2 < \Delta BIC < 6$, the evidence against the model with higher BIC is positive; (3) if $6 < \Delta BIC < 10$, the evidence against the model with higher BIC is strong; (4) if $10 < \Delta BIC$, the evidence against the model with higher BIC is very strong.

3. DERIVATION OF THE PHYSICAL PARAMETERS WITHIN THE FIREBALL MODELS

The initial Lorentz factor of a GRB jet is a very important parameter for understanding GRB physics, and is also very difficult to measure for most GRBs (Zhang 2018). In general, there are three methods that have been proposed to estimate the Lorentz factor. The first one is to use the high-energy cutoff of the prompt gamma-ray spectrum, which is from the pair production when the absorption optical depth is close to one (Fenimore et al. 1993; Lithwick & Sari 2001; Zhang & Pe'er 2009). The second approach to estimating the Lorentz factor is using the early afterglow light curves with a smooth onset bump that shows the signal of fireball deceleration (Sari & Piran 1999; Kobayashi & Zhang 2007; Liang et al. 2010). The third one is using the blackbody component detected in some GRB spectra (Pe'er et al. 2007; Ryde et al. 2010; Gao & Zhang 2015). In this section, we derive the physical parameters based on the observed thermal component in prompt emission of GRB 211211A, such as the Lorentz factor (Γ_{ph}) and the radius of the photosphere (R_{ph}). We also calculate the magnetization factor (σ_0) and dimensionless entropy (η) by assuming the hybrid jet of GRB 211211A.

3.1. *Lorentz Factor and Photosphere Radius*

In our analyses, the time-resolved spectra of the GRB 211211A prompt emission is composed of a thermal component (BB component) and a nonthermal component 2SBPL component). Following the method of Pe'er et al. (2007), we estimate the Γ_{ph} and R_{ph} with the BB component derived from our spectral fits in different time slices;

$$\Gamma_{\mathrm{ph}} = \left[(1.06)(1+z)^2 D_{\mathrm{L}} \frac{Y \sigma_{\mathrm{T}} F_{\mathrm{obs}}}{2 m_{\mathrm{p}} c^3 \Re}\right]^{1/4} \quad (6)$$

where D_{L} is the luminosity distance, m_{p} is the proton mass, σ_{T} is the Thomson scattering cross section, and F_{obs} is the observed total flux. In our calculation, we fix the $Y = 1$, which is the ratio between the total fireball energy and the energy emitted in the γ-ray. The definition of $\Re$ is written as

$$\Re \equiv \left(\frac{F_{BB}}{\sigma T^4}\right)^{1/2} \quad (7)$$

where σ and F_{BB} are the Stefan's constant and the observed blackbody component flux, respectively. On the other hand, the R_{ph} can be expressed as

$$R_{ph} = \left(L \sigma_T / 8\pi \Gamma_{ph}^3 m_p c^3\right) \quad (8)$$

where $L = 4\pi D_L^2 F_{\mathrm{obs}}$ is the luminosity that is measured for bursts with known redshift. The calculation results are shown in Table 3.

Figure 4 shows the temporal evolution of Γ_{ph} and R_{ph}. During main emission phase, the evolution of Γ_{ph} is initially tracking with the light curve, and maximum value can be reached as high as 311 at the peak of the light curve. In the extended emission phase, the Γ_{ph} seems to be also tracking with the light curve, and it peaked at

$\Gamma_{\rm ph} = 197$, then, it is gradually going down to 91 until it reaches the end of extended emission. As for the $R_{\rm ph}$, the highest value of $R_{\rm ph}$ is around $\sim 2.71 \times 10^{10}$ cm and it keeps fluctuating around $\sim 10^{10}$ cm.

3.2. *Magnetization parameter and dimensionless entropy*

One is different from the method of Pe'er et al. (2007) who inferred the central engine parameters by using the observed data within the framework of a pure fireball shock model. Gao & Zhang (2015) proposed a hybrid relativistic outflow of GRB (e.g., hot fireball component and Poynting-flux component), and developed a theory of its photosphere emission. One interesting question is that the observed nonthermal component of GRB 211211A is from the internal shock of a fireball or another cold Poynting-flux component. Here, we infer the magnetization factor (σ_0) and dimensionless entropy (η) by assuming the hybrid jet of GRB 211211A.

The magnetization factor σ_0 is defined as $\sigma_0 = L_{\rm c}/L_{\rm h}$, where the $L_{\rm h}$ and $L_{\rm c}$ are the luminosity of the hot fireball component and cold Poynting-flux component, respectively. The dimensionless entropy η can be defined as $\eta = L_{\rm h}/\dot{M}c^2$, where $\dot{M}$ is the accretion rate. The time varying of the (η, σ_0) pair at the central engine can result in the evolution of the photosphere emission proprieties. Based on the results of derivation in Gao & Zhang (2015), several situations of different (η, σ_0) pairs are considered; (1) $\eta \gg 1, \sigma_0 \ll 1$: it means that the photosphere emission is dominated by a pure fireball component; (2) $\eta \sim 1, 1+\sigma_0 \gg 1$: a Poynting-flux-dominated outflow; no detection of any thermal component in the GRB spectrum. By invoking the 'top-down' approach and based on the judgment criteria proposed by Gao & Zhang (2015), we can infer the parameters of the central engine by using the observed quasi-thermal photosphere emission parameters (such as $F_{\rm BB}$, $F_{\rm obs}$, and kT). However, the inferred parameters of the central engine are sensitively dependent on the selected initial radius (r_0) of the central engine. For convenience, we adopt the initial radius $r_0 = 10^7$ cm, and one can obtain all the photosphere characteristic parameters of the hybrid model (e.g., η, $1+\sigma_0$, $R_{\rm ph}$, $\Gamma_{\rm ph}$, and $1+\sigma_{\rm ph}$). Here, $1+\sigma_{\rm ph}$ is the magnetization parameter at $R_{\rm ph}$. Table 4 shows the derived parameters of GRB 211211A in a hybrid jet model.

Figure 4 also shows the comparisons of $\Gamma_{\rm ph}$ and $R_{\rm ph}$ evolution for both the pure fireball model and hybrid jet model with fixed $r_0 = 10^7$ cm. It is interesting that the $\Gamma_{\rm ph}$ evolution behavior of a pure fireball model is similar to that of the hybrid jet model, and the evolution of $R_{\rm ph}$ is matched very well between those two models. Figure 5 presents the temporal evolution of $1+\sigma_0$ and η in the central engine with $r = r_0$, as well as $1+\sigma_{\rm ph}$ at $R_{\rm ph}$. The values of $1+\sigma_0$ and η are larger than 1 and 10 for different time slices, respectively. It means that at least the Poynting-flux component is indeed existent in the central engine. Meanwhile, it is clear to see that the values of $1+\sigma_{\rm ph}$ are larger than 1 for different time slices, and range in [1-50]. So that, those results suggest that the Poynting-flux component should always be a presence at the position of the central engine and photosphere radius. The observed thermal and nonthermal components in GRB 211211A seem to be from the contributions of hot fireball and Poynting-flux outflow, respectively.

3.3. $\Gamma_{\rm ph}$ - $E_{\gamma,\rm iso}/L_{\gamma,\rm iso}$ *correlations*

Liang et al. (2010) discovered a tight correlation between initial Lorentz factor Γ_0 and isotropic γ-ray energy $E_{\gamma,\rm iso}$, namely $\Gamma_0 \propto E_{\gamma,\rm iso}^{0.25}$. Lü et al. (2012) also found another tight correlation of Γ_0 and isotropic γ-ray luminosity $L_{\gamma,\rm iso}$, e.g., $\Gamma_0 \propto L_{\gamma,\rm iso}^{0.3}$. Those two correlations can be interpreted well by using a neutrino-cooled hyperaccretion disk around a stellar mass black hole as the GRB central engine (Lü et al. 2012).

In order to test whether the $\Gamma_{\rm ph}$ from time-resolved BB emission and $E_{\gamma,\rm iso}/L_{\gamma,\rm iso}$ of GRB 211211A are tracking similar correlations to the above, Figure 6 shows the relationship between $\Gamma_{\rm ph}$ and $E_{\gamma,\rm iso}/L_{\gamma,\rm iso}$. We caution the reader that we do not adopt the data from Liang et al. (2010) and Lü et al. (2012) to do the joint fitting, because they adopt different methods to estimate the Lorentz factor. However, we collect the data of time-resolved spectra in GRB 160625B, which have the thermal emission and use the same method (e.g., BB emission) to infer the Lorentz factor. So, we used $\Gamma_{\rm ph}$ in our fitting to replace Γ_0 in Liang et al. (2010), and the data of GRB 160625B are taken from Wang et al. (2017). For the diagram of $\Gamma_{\rm ph} - L_{\gamma,\rm iso}$, we make a joint fitting of the two groups (GRB 160626B and GRB 211211A) with a power-law model and find $\Gamma_{\rm ph} \propto L_{\gamma,\rm iso}^{0.24\pm0.01}$ with a Pearsons correlation coefficient of 0.96 and $\rm p < 10^{-4}$. Also, applying the power-law fitting to $\Gamma_{\rm ph} - E_{\gamma,\rm iso}$, we find $\Gamma_{\rm ph} \propto E_{\gamma,\rm iso}^{0.26\pm0.02}$ with a Pearsons correlation coefficient of 0.91 and $\rm p < 10^{-4}$. Those two results are similar to that of Lü et al. (2012) and Liang et al. (2010), respectively. It suggests that the central engine of GRB 211211A may be a stellar mass black hole with a neutrino-cooled hyperaccretion disk.

4. CONCLUSION AND DISCUSSION

GRB 211211A was observed by Fermi/GBM, Swift/BAT, and Insight-HXMT to have a duration of ~ 84 seconds at redshift z =0.076, but the light curve is characterized by an initial hard-main emission (with a duration ~ 13 s) followed by a series of soft gamma-ray extended emission with a duration ~ 55 s. The structure of the light curve is similar to the cases of GRB 060614 and GRB 211227A, which are believed to be from the compact star merger (Yang et al. 2022; Xiao et al. 2022; Lü et al. 2022). The total isotropic-equivalent energy ($E_{\gamma,\rm iso}$) and luminosity ($L_{\gamma,\rm iso}$) are as high as 7.6×10^{51} erg and 1.9×10^{51} erg s^{-1}, respectively. At such low redshift, it is surprising that deep searches of an underlying SN give null results, but being associated with a kilonova is observed by several optical telescopes (Rastinejad et al. 2022). That observed evidence suggests that GRB 211211A is originated from a binary compact star merger (Rastinejad et al. 2022; Yang et al. 2022; Xiao et al. 2022; Gompertz et al. 2022).

By reanalyzing the data observed with the GBM on board the Fermi mission, we find the following interesting results:

- We find that the 2SBPL+BB model is the best

one to adequately describe the observed data in both time-integrated and time-resolved spectra in the prompt emission of GRB 211211A based on the BIC criterion, and it means that both thermal and nonthermal components in GRB 211211A should be a significant presence.

- The behavior of temporal evolution of $E_{\rm b}$, $E_{\rm pk}$ for the 2SBPL function and kT for BB emission seem to be tracking with pulses of the light curve.

- By inferring the Lorentz factor $\Gamma_{\rm ph}$ and photosphere radius $R_{\rm ph}$ based on the observed BB emission within the framework of a pure fireball model, we find that the temporal evolution of $\Gamma_{\rm ph}$ seems to be tracking with the light curve, and its range from 87 to 311. However, the highest value of $R_{\rm ph}$ is around $\sim 2.7\times10^{10}$ cm and it keeps fluctuating around $\sim 10^{10}$ cm.

- By calculating the magnetization factor σ_0 in the central engine and $\sigma_{\rm ph}$ at the photosphere radius within the framework of the hybrid jet model, we find that the values of both $1+\sigma_0$ and $1+\sigma_{\rm ph}$ are larger than 1 for different time slices for fixed initial $r_0 = 10^7$ cm, and its range of [1,120]. It means that at least the Poynting-flux component is indeed existent in both the central engine and photosphere radius.

- Moreover, we also plot the diagrams of $\Gamma_{\rm ph}$-$E_{\gamma,\rm iso}/L_{\gamma,\rm iso}$, and find the relationships as $\Gamma_{\rm ph}\propto E_{\gamma,\rm iso}^{0.26\pm0.02}$ and $\Gamma_{\rm ph}\propto L_{\gamma,\rm iso}^{0.24\pm0.01}$ for the time-resolved spectral data of GRB 211211A. Those two correlations are consistent with that of in Liang et al. (2010) and Lü et al. (2012), respectively. It suggests that the central of GRB 211211A may be a stellar mass black hole with a neutrino-cooled hyperaccretion disk.

If the central engine of GRB 211211A is a stellar mass black hole that is formed from a binary compact star merger (Gao et al. 2022). Lei et al. (2017) proposed that two jet launching mechanisms, i.e., $\nu\bar{\nu}$ annihilation and the Blandford-Znajek (BZ; Blandford & Znajek 1977) process, are indeed considered to power thermal and nonthermal components in the relativistic jet, respectively; the $\nu\bar{\nu}$ annihilation mechanism liberates the gravitational energy from the accretion disk, and the BZ mechanism extracts the spin energy from the Kerr black hole (Popham et al. 1999; Lee et al. 2000; Li & Paczyński 2000; Gu et al. 2006; Lei et al. 2009, 2013). In this scenario, the observed thermal and nonthermal emissions in GRB 211211A can be interpreted as follows. The jet of GRB 211211A can be launched from a hyperaccreting black hole via $\nu\bar{\nu}$ annihilation and the BZ mechanism. Initially, due to a very high accretion rate of the black hole, the $\nu\bar{\nu}$ annihilation should be dominated. It can produce thermal emission when the photons escape the system at the photosphere radius, and the internal shock or Poynting-flux outflow is used to produce the nonthermal component. After tens of seconds, the $\nu\bar{\nu}$ annihilation is not strong enough along with the decreasing of accretion rate. But the magnetic field of the black hole becomes gradually stronger due to storage time, and the BZ mechanism will be dominated. If this is the case, it is natural to explain the observed gradually decreased thermal emission and gradually increased nonthermal emission of GRB 211211A.

Alternatively, what we discussed above about the evidence of Poynting-flux existence (e.g., magnetization factor σ_0) in our results is dependent on the selected R_0 in the calculations of the hybrid model, and we fixed $R_0 = 10^7$ cm in our calculations. For different selected R_0, such as $R_0 = 10^8$ cm or $R_0 = 10^9$ cm, it corresponds to different values of σ_0. So, it is difficult to judge whether it is accompanied by the Poynting-flux component in the jet. If this is the case, only $\nu\bar{\nu}$ annihilation mechanism can interpret the observed thermal emission (from the photosphere) and nonthermal emission (from the internal shock).

To find out such a uniform model to explain all observed characteristics of GRB 211211A, of course, is not an easy task. We therefore encourage intense multi-band follow-up observations for GRB 211211A-like events in the future.

We are very grateful to thank the referee for helpful comments and suggestions to improve this manuscript. We acknowledge the use of the public data from the Fermi/GBM data archive. This work is supported by the National Natural Science Foundation of China (grant Nos. 11922301, and 12133003), the Program of Bagui Young Scholars Program (LHJ), and the Guangxi Science Foundation (grant No. 2017GXNSFFA198008).

REFERENCES

Abdo, A. A., Ackermann, M., Ajello, M., et al. 2009, ApJ, 706, L138. doi:10.1088/0004-637X/706/1/L138
Axelsson, M., Baldini, L., Barbiellini, G., et al. 2012, ApJ, 757, L31. doi:10.1088/2041-8205/757/2/L31
Band, D., Matteson, J., Ford, L., et al. 1993, ApJ, 413, 281. doi:10.1086/172995
Berger, E. 2014, ARA&A, 52, 43.
Blandford, R. D. & Znajek, R. L. 1977, MNRAS, 179, 433. doi:10.1093/mnras/179.3.433
Bucciantini, N., Metzger, B. D., Thompson, T. A., et al. 2012, MNRAS, 419, 1537. doi:10.1111/j.1365-2966.2011.19810.x
D'Ai, A., Ambrosi, E., D'Elia, V., et al. 2021, GRB Coordinates Network, Circular Service, No. 31202, 1
Dai, Z. G. & Lu, T. 1998a, MNRAS, 298, 87. doi:10.1046/j.1365-8711.1998.01681.x
Dai, Z. G. & Lu, T. 1998b, A&A, 333, L87
Eichler, D., Livio, M., Piran, T., et al. 1989, Nature, 340, 126. doi:10.1038/340126a0
Fenimore, E. E., Epstein, R. I., & Ho, C. 1993, A&AS, 97, 59
Gao, H. & Zhang B et al. 2015, ApJ, 801, 5. doi:0.1088/0004-637X/801/2/103
Gao, H., Lei, W.-H., & Zhu, Z.-P. 2022, ApJ, 934, L12. doi:10.3847/2041-8213/ac80c7
Gompertz, B. P., Ravasio, M. E., Nicholl, M., et al. 2022, Nature Astronomy. doi:10.1038/s41550-022-01819-4
Goodman, J. 1986, ApJ, 308, L47. doi:10.1086/184741
Guiriec, S., Connaughton, V., Briggs, M. S., et al. 2011, ApJ, 727, L33. doi:10.1088/2041-8205/727/2/L33
Guiriec, S., Daigne, F., Hascoët, R., et al. 2013, ApJ, 770, 32. doi:10.1088/0004-637X/770/1/32
Gu, W.-M., Liu, T., & Lu, J.-F. 2006, ApJ, 643, L87. doi:10.1086/505140

TABLE 1
Time-integral spectral analysis results of GRB 211211A.

$t_1 - t_2$ (s)	Model	$\alpha(\alpha_1)$	$E_{\rm b}$ (keV)	$E_{\rm p}/E_{\rm c}$ (keV)	β	α_2	kT (keV)	BIC	favorite Model
0.5-70	Band	$-1.22^{+0.01}_{-0.01}$	...	497^{+15}_{-15}	$-2.21^{+0.03}_{-0.03}$	...	...	8633	
	CPL	$-1.27^{+0.01}_{-0.01}$	...	916^{+19}_{-19}	...	...	...	8964	
	BB	...	...	...	...	...	53	125651	
	Band+BB	$-1^{+0.01}_{-0.01}$	...	175^{+6}_{-6}	$-2.06^{+0.02}_{-0.02}$	...	201^{+7}_{-7}	7864	
	CPL+BB	$-1.08^{+0.01}_{-0.01}$	...	250^{+5}_{-5}	...	...	312^{+5}_{-5}	8149	
	SBPL	$-1.19^{+0.01}_{-0.01}$	210^{+10}_{-11}	...	$-2.11^{+0.02}_{-0.02}$	...	...	8523	
	SBPL+BB	$-0.96^{+0.02}_{-0.02}$	81^{+4}_{-4}	...	$-2.08^{+0.02}_{-0.02}$	...	199^{+6}_{-6}	7732	
	2SBPL	$-0.6^{+0.04}_{-0.04}$	$26.2^{+1.3}_{-1.3}$	1020^{+40}_{-50}	$-2.93^{+0.07}_{-0.07}$	$-1.59^{+0.01}_{-0.01}$	...	7461	
	2SBPL+BB	$-0.6^{+0.04}_{-0.04}$	$27^{+1.9}_{-1.8}$	1200^{+110}_{-110}	$-3.14^{+0.14}_{-0.13}$	$-1.62^{+0.02}_{-0.02}$	77^{+16}_{-15}	7443	$\surd$

Hou, S.-J., Zhang, B.-B., Meng, Y.-Z., et al. 2018, ApJ, 866, 13. doi:10.3847/1538-4357/aadc07

Kumar, P. & Zhang, B. 2015, Phys. Rep., 561, 1. doi:10.1016/j.physrep.2014.09.008

Kobayashi, S. & Zhang, B. 2007, ApJ, 655, 973. doi:10.1086/510203

Lee, H. K., Wijers, R. A. M. J., & Brown, G. E. 2000, Phys. Rep., 325, 83. doi:10.1016/S0370-1573(99)00084-8

Lei, W. H., Wang, D. X., Zhang, L., et al. 2009, ApJ, 700, 1970. doi:10.1088/0004-637X/700/2/1970

Lei, W.-H., Zhang, B., & Liang, E.-W. 2013, ApJ, 765, 125. doi:10.1088/0004-637X/765/2/125

Lei, W.-H., Zhang, B., Wu, X.-F., et al. 2017, ApJ, 849, 47. doi:10.3847/1538-4357/aa9074

Li, L.-X. & Paczyński, B. 2000, ApJ, 534, L197. doi:10.1086/312678

Li, L. 2019, ApJS, 242, 16.

Liang, E.-W., Yi, S.-X., Zhang, J., et al. 2010, ApJ, 725, 2209. doi:10.1088/0004-637X/725/2/2209

Lithwick, Y. & Sari, R. 2001, ApJ, 555, 540. doi:10.1086/321455

Lü, H.-J., Lü, J., Zhong, S.-Q., et al. 2017, ApJ, 849, 71. doi:10.3847/1538-4357/aa8f99

Lü, H.-J. & Zhang, B. 2014, ApJ, 785, 74. doi:10.1088/0004-637X/785/1/74

Lü, H.-J., Zhang, B., Lei, W.-H., et al. 2015, ApJ, 805, 89. doi:10.1088/0004-637X/805/2/89

Lü, H.-J., Yuan, H.-Y., Yi, T.-F., et al. 2022, ApJ, 931, L23. doi:10.3847/2041-8213/ac6e3a

Lü, J., Zou, Y.-C., Lei, W.-H., et al. 2012, ApJ, 751, 49. doi:10.1088/0004-637X/751/1/49

Kaneko, Y., Preece, R. D., Briggs, M. S., et al. 2006, ApJS, 166, 298.

Mangan, J., Dunwoody, R., Meegan, C., et al. 2021, GRB Coordinates Network, Circular Service, No. 31210, 1

Meegan, C., Lichti, G., Bhat, P. N., et al. 2009, ApJ, 702, 791. doi:10.1088/0004-637X/702/1/791

Metzger, B. D., Giannios, D., Thompson, T. A., et al. 2011, MNRAS, 413, 2031. doi:10.1111/j.1365-2966.2011.18280.x

Mészáros, P. & Rees, M. J. 1997, ApJ, 476, 232. doi:10.1086/303625

Mészáros, P. 2002, ARA&A, 40, 137. doi:10.1146/annurev.astro.40.060401.093821

Narayan, R., Piran, T., & Kumar, P. 2001, ApJ, 557, 949. doi:10.1086/322267

Neath, A. A. & Cavanaugh, J. E. 2012, WIREs Comput. Stat., 4, 199. doi: 10.1002/wics.199

Paczynski, B. 1986, ApJ, 308, L43. doi:10.1086/184740

Pe'er, A., Ryde, F., Wijers, R. A. M. J., et al. 2007, ApJ, 664, L1. doi:10.1086/520534

Popham, R., Woosley, S. E., & Fryer, C. 1999, ApJ, 518, 356. doi:10.1086/307259

Ravasio, M. E., Oganesyan, G., Ghirlanda, G., et al. 2018, A&A, 613, A16.

Rastinejad, J. C., Gompertz, B. P., Levan, A. J., et al. 2022, Nature, 612, 223. doi:10.1038/s41586-022-05390-w

Rees, M. J. & Meszaros, P. 1994, ApJ, 430, L93. doi:10.1086/187446

Ryde, F. 2005, ApJ, 625, L95. doi:10.1086/431239

Ryde, F., Axelsson, M., Zhang, B. B., et al. 2010, ApJ, 709, L172. doi:10.1088/2041-8205/709/2/L172

Sari, R., Piran, T., & Narayan, R. 1998, ApJ, 497, L17. doi:10.1086/311269

Sari, R. & Piran, T. 1999, A&AS, 138, 537. doi:10.1051/aas:1999342

Thompson, C. 1994, MNRAS, 270, 480. doi:10.1093/mnras/270.3.480

Usov, V. V. 1992, Nature, 357, 472. doi:10.1038/357472a0

Vianello, G., Lauer, R. J., Burgess, J. M., et al. 2017, Proceedings of the 7th International Fermi Symposium, 130

Wang, Y.-Z., Wang, H., Zhang, S., et al. 2017, ApJ, 836, 81. doi:10.3847/1538-4357/aa56c6

Xiao, S., Zhang, Y,-Q., Zhu, Z,-P., et al.2022, arXiv:2205.02186

Yang, J., Ai, S., Zhang, B.-B., et al. 2022, Nature, 612, 232. doi:10.1038/s41586-022-05403-8

Zhang, B. 2018, The Physics of Gamma-Ray Bursts by Bing Zhang. ISBN: 978-1-139-22653-0. Cambridge Univeristy Press, 2018. doi:10.1017/9781139226530

Zhang, B. & Pe'er, A. 2009, ApJ, 700, L65. doi:10.1088/0004-637X/700/2/L65

Zhang, B. & Mészáros, P. 2001, ApJ, 552, L35. doi:10.1086/320255

Zhang, B. & Mészáros, P. 2004, International Journal of Modern Physics A, 19, 2385. doi:10.1142/S0217751X0401746X

Zhang, B. & Yan, H. 2011, ApJ, 726, 90. doi:10.1088/0004-637X/726/2/90

Zhang, B., Lü, H.-J., & Liang, E.-W. 2016, Space Sci. Rev., 202, 3. doi:10.1007/s11214-016-0305-9

Zhang, B.-B., Zhang, B., Liang, E.-W., et al. 2011, ApJ, 730, 141. doi:10.1088/0004-637X/730/2/141

Zhang, B.-B., Zhang, B., Castro-Tirado, A. J., et al. 2018, Nature Astronomy, 2, 69. doi:10.1038/s41550-017-0309-8

Zhang, Y. Q., Xiong, S. L., Li, X. B., et al. 2021, GRB Coordinates Network, Circular Service, No. 31236, 1

TABLE 2
THE FITTING RESULTS OF TIME-RESOLVED SPECTRA WITH 2SBPL AND 2SBPL+BB IN GRB 211211A PROMPT EMISSION.

t_1	t_2	2SBPL					BIC (PGSTAT)	2SBPL + BB						BIC (PGSTAT)	ΔBIC
s	s	α_1	α_2	$E_{\rm b}$(keV)	$E_{\rm pk}$(keV)	β		α_1	α_2	$E_{\rm b}$(keV)	$E_{\rm pk}$(keV)	β	kT(keV)		
0.5	1.5	$-0.9^{+0.5}_{-0.5}$	$-1.1^{+0.6}_{-0.5}$	13^{+10}_{-9}	151^{+24}_{-60}	$-2.9^{+0.5}_{-0.5}$	1640.4(1605.2)	$-0.9^{+0.5}_{-0.4}$	$-1.1^{+0.5}_{-0.5}$	13^{+9}_{-9}	121^{+24}_{-40}	$-3.1^{+0.5}_{-0.5}$	46^{+19}_{-19}	1632.6(1585.7)	7.8
1.5	2.5	$-0.9^{+0.4}_{-0.5}$	$-1.07^{+0.4}_{-0.33}$	26^{+15}_{-13}	820^{+120}_{-120}	$-2.52^{+0.14}_{-0.15}$	2001.2(1966.1)	$-0.83^{+0.34}_{-0.5}$	$-1.17^{+0.5}_{-0.3}$	27^{+12}_{-12}	980^{+210}_{-210}	$-2.66^{+0.22}_{-0.22}$	65^{+18}_{-19}	1999.9(1953.1)	1.3
2.5	3.5	$-0.73^{+0.9}_{-0.01}$	$-1.48^{+0.1}_{-0.1}$	98^{+18}_{-19}	1370^{+130}_{-130}	$-3.2^{+0.16}_{-0.17}$	2594.7(2559.5)	$-0.67^{+0.04}_{-0.04}$	$-1.64^{+0.04}_{-0.04}$	92^{+12}_{-12}	2100^{+210}_{-210}	$-3.99^{+0.31}_{-0.31}$	168^{+17}_{-16}	2569.5(2522.6)	25.2
3.5	4.5	$-0.6^{+0.4}_{-0.8}$	$-1.09^{+0.8}_{-0.34}$	38^{+5}_{-5}	840^{+150}_{-100}	$-2.88^{+0.09}_{-0.09}$	2327.8(2292.6)	$-0.61^{+0.33}_{-0.8}$	$-1.21^{+0.8}_{-0.35}$	42^{+7}_{-7}	960^{+190}_{-190}	$-2.99^{+0.18}_{-0.14}$	100^{+40}_{-40}	2326(2279.1)	1.8
4.5	5.5	$-0.68^{+0.13}_{-0.12}$	$-1.66^{+0.06}_{-0.08}$	38^{+9}_{-9}	530^{+80}_{-80}	$-3.2^{+0.4}_{-0.4}$	2102.9(2067.7)	$-0.69^{+0.12}_{-0.11}$	$-1.71^{+0.08}_{-0.08}$	39^{+9}_{-9}	570^{+110}_{-110}	$-3.3^{+0.4}_{-0.4}$	73^{+26}_{-30}	2095.1(2048.2)	7.8
5.5	6.5	$-0.62^{+0.04}_{-0.03}$	$-1.55^{+0.02}_{-0.03}$	81^{+9}_{-9}	1700^{+100}_{-100}	$-3.36^{+0.14}_{-0.14}$	2592.3(2557.2)	$-0.59^{+0.05}_{-0.04}$	$-1.55^{+0.24}_{-0.04}$	72^{+9}_{-9}	1860^{+170}_{-160}	$-3.48^{+0.17}_{-0.18}$	126^{+40}_{-35}	2579.9(2533.1)	12.4
6.5	7.5	$-0.57^{+0.12}_{-0.03}$	$-1.35^{+0.05}_{-0.1}$	70^{+7}_{-7}	1630^{+70}_{-110}	$-3.09^{+0.09}_{-0.09}$	2751.6(2716.4)	$-0.69^{+0.25}_{-0.7}$	$-1.22^{+0.7}_{-0.24}$	67^{+7}_{-7}	1750^{+280}_{-190}	$-3.12^{+0.1}_{-0.1}$	100^{+60}_{-50}	2743.6(2696.7)	8
7.5	8.5	$0.68^{+0.29}_{-0.8}$	$-1.21^{+0.8}_{-0.28}$	57^{+5}_{-5}	1440^{+270}_{-160}	$-3.34^{+0.13}_{-0.31}$	2539.6(2504.4)	$-0.56^{+0.2}_{-0.05}$	$-1.35^{+0.09}_{-0.2}$	55^{+6}_{-6}	1670^{+180}_{-180}	$-3.64^{+0.21}_{-0.22}$	136^{+24}_{-23}	2524.6(2477.7)	15
8.5	9.5	$-0.5^{+0.11}_{-0.11}$	$-1.67^{+0.04}_{-0.05}$	34^{+5}_{-5}	660^{+90}_{-90}	$-3.2^{+0.35}_{-0.4}$	2090.2(2055.1)	$-0.51^{+0.11}_{-0.11}$	$-1.69^{+0.05}_{-0.06}$	35^{+5}_{-5}	650^{+120}_{-100}	$-3.2^{+0.4}_{-0.4}$	80^{+50}_{-40}	2080.5(2033.7)	9.7
9.5	10.5	$-0.33^{+0.11}_{-0.11}$	$-1.75^{+0.04}_{-0.04}$	$33.4^{+3.2}_{-3.2}$	680^{+120}_{-130}	$-3.2^{+0.4}_{-0.4}$	2072.5(2037.3)	$-0.34^{+0.11}_{-0.11}$	$-1.76^{+0.04}_{-0.04}$	$33.8^{+3.4}_{-3.4}$	690^{+160}_{-140}	$-3.2^{+0.4}_{-0.4}$	64^{+31}_{-33}	2066.6(2019.8)	5.9
10.5	11.5	$-0.41^{+0.12}_{-0.12}$	$-1.8^{+0.04}_{-0.04}$	$31^{+3.1}_{-3}$	590^{+90}_{-100}	$-3.9^{+0.5}_{-0.5}$	1991.1(1955.9)	$-0.44^{+0.12}_{-0.12}$	$-1.85^{+0.07}_{-0.08}$	32^{+4}_{-4}	530^{+150}_{-170}	$-3.8^{+0.5}_{-0.5}$	90^{+50}_{-50}	1981.1(1934.3)	10
11.5	12.5	$-0.68^{+0.21}_{-0.19}$	$-1.82^{+0.07}_{-0.14}$	26^{+6}_{-5}	410^{+170}_{-220}	$-3^{+0.7}_{-0.7}$	1850.3(1815.1)	$-0.68^{+0.16}_{-0.17}$	$-1.89^{+0.06}_{-0.08}$	27^{+5}_{-5}	450^{+220}_{-250}	$-3.1^{+0.6}_{-0.6}$	50^{+23}_{-22}	1843.1(1796.2)	7.2
12.5	13.5	$-0.56^{+0.32}_{-0.32}$	$-1.83^{+0.1}_{-0.12}$	21^{+5}_{-5}	540^{+280}_{-350}	$-2.9^{+0.6}_{-0.6}$	1711.8(1676.6)	$-0.53^{+0.3}_{-0.29}$	$-1.86^{+0.09}_{-0.11}$	20^{+5}_{-4}	570^{+300}_{-400}	$-2.9^{+0.6}_{-0.6}$	45^{+18}_{-18}	1703.9(1657.1)	7.9
13.5	15	$-0.63^{+0.23}_{-0.25}$	$-1.88^{+0.07}_{-0.08}$	22^{+4}_{-4}	500^{+270}_{-310}	$-3^{+0.6}_{-0.6}$	2154.1(2118.8)	$-0.65^{+0.24}_{-0.23}$	$-1.86^{+0.05}_{-0.12}$	21^{+4}_{-4}	530^{+320}_{-350}	$-3^{+0.6}_{-0.6}$	43^{+18}_{-18}	2152.1(2105.3)	2
15	17	$-0.53^{+0.19}_{-0.17}$	$-1.81^{+0.05}_{-0.13}$	26^{+4}_{-4}	600^{+270}_{-310}	$-2.8^{+0.5}_{-0.6}$	2624.1(2588.8)	$-0.52^{+0.15}_{-0.16}$	$-1.88^{+0.06}_{-0.07}$	$26.1^{+3.5}_{-3.3}$	670^{+310}_{-350}	$-2.9^{+0.6}_{-0.6}$	46^{+21}_{-20}	2618.4(2571.6)	5.7
17	19	$-0.5^{+0.1}_{-0.1}$	$-1.71^{+0.04}_{-0.04}$	32^{+4}_{-4}	560^{+70}_{-70}	$-3.31^{+0.34}_{-0.35}$	2860.4(2825.2)	$-0.52^{+0.1}_{-0.1}$	$-1.74^{+0.05}_{-0.05}$	33^{+4}_{-4}	570^{+90}_{-80}	$-3.33^{+0.4}_{-0.35}$	67^{+40}_{-35}	2853.4(2806.6)	7
19	21	$-0.63^{+0.13}_{-0.13}$	$-1.75^{+0.08}_{-0.09}$	33^{+7}_{-6}	450^{+90}_{-90}	$-3^{+0.4}_{-0.4}$	2781.7(2746.5)	$-0.66^{+0.1}_{-0.1}$	$-1.81^{+0.08}_{-0.08}$	35^{+6}_{-6}	530^{+150}_{-140}	$-3.2^{+0.5}_{-0.5}$	60^{+22}_{-23}	2774.5(2727.7)	7.2
21	23	$-0.57^{+0.1}_{-0.1}$	$-1.79^{+0.05}_{-0.05}$	31^{+4}_{-4}	350^{+50}_{-50}	$-3.2^{+0.31}_{-0.32}$	2822.7(2787.5)	$-0.59^{+0.09}_{-0.1}$	$-1.84^{+0.07}_{-0.08}$	33^{+4}_{-4}	350^{+80}_{-70}	$-3.2^{+0.4}_{-0.4}$	68^{+23}_{-27}	2814.3(2767.5)	8.4
23	25	$-0.52^{+0.1}_{-0.1}$	$-1.75^{+0.05}_{-0.05}$	31^{+4}_{-4}	390^{+50}_{-50}	$-3.25^{+0.32}_{-0.31}$	2836.4(2801.2)	$-0.53^{+0.11}_{-0.11}$	$-1.78^{+0.06}_{-0.06}$	32^{+4}_{-4}	410^{+80}_{-70}	$-3.3^{+0.4}_{-0.4}$	62^{+22}_{-27}	2829.1(2782.2)	7.3
25	27	$-0.53^{+0.12}_{-0.12}$	$-1.86^{+0.05}_{-0.05}$	$28.1^{+3.3}_{-3.4}$	330^{+70}_{-70}	$-3.6^{+0.5}_{-0.5}$	2718.9(2683.7)	$-0.54^{+0.12}_{-0.12}$	$-1.87^{+0.06}_{-0.06}$	$28.1^{+3.4}_{-3.4}$	290^{+90}_{-100}	$-3.5^{+0.6}_{-0.6}$	63^{+40}_{-32}	2706.8(2660.1)	12.1
27	29	$-0.56^{+0.17}_{-0.18}$	$-1.78^{+0.2}_{-0.17}$	22^{+4}_{-5}	108^{+30}_{-27}	$-3.1^{+0.6}_{-0.6}$	2643.6(2608.4)	$-0.7^{+0.5}_{-0.6}$	$-1.1^{+0.7}_{-0.6}$	14^{+8}_{-7}	76^{+11}_{-15}	$-2.69^{+0.25}_{-0.19}$	69^{+14}_{-13}	2628.7(2581.9)	14.9
29	31	$-0.81^{+0.32}_{-0.3}$	$-0.9^{+0.4}_{-0.4}$	15^{+9}_{-9}	64^{+5}_{-5}	$-2.29^{+0.06}_{-0.06}$	2601.8(2566.6)	$-0.88^{+0.4}_{-0.31}$	$-0.8^{+0.4}_{-0.4}$	13^{+7}_{-7}	62^{+5}_{-5}	$-2.31^{+0.07}_{-0.06}$	45^{+17}_{-19}	2594.1(2547.2)	7.7
31	33	$-0.37^{+0.24}_{-0.24}$	$-1.81^{+0.18}_{-0.15}$	$15.5^{+2.4}_{-2.5}$	75^{+19}_{-18}	$-2.8^{+0.4}_{-0.4}$	2616.2(2581)	$-0.8^{+0.5}_{-0.5}$	$-1.2^{+0.7}_{-0.7}$	12^{+5}_{-5}	58^{+9}_{-10}	$-2.6^{+0.23}_{-0.22}$	63^{+21}_{-20}	2605.6(2558.8)	10.6
33	35	$-0.45^{+0.27}_{-0.23}$	$-1.72^{+0.14}_{-0.21}$	21^{+5}_{-5}	116^{+28}_{-27}	$-3^{+0.5}_{-0.5}$	2633.9(2598.7)	$-0.51^{+0.32}_{-0.24}$	$-1.59^{+0.19}_{-0.34}$	20^{+5}_{-5}	105^{+28}_{-29}	$-2.9^{+0.4}_{-0.4}$	49^{+21}_{-21}	2627.4(2580.5)	6.5
35	37	$-0.56^{+0.15}_{-0.15}$	$-1.89^{+0.05}_{-0.06}$	$24.9^{+3.3}_{-3.1}$	230^{+50}_{-60}	$-3.6^{+0.6}_{-0.6}$	2640.5(2605.3)	$-0.55^{+0.13}_{-0.14}$	$-1.91^{+0.06}_{-0.06}$	$24.9^{+2.8}_{-2.8}$	190^{+70}_{-80}	$-3.4^{+0.6}_{-0.6}$	60^{+28}_{-28}	2631.5(2584.6)	9
37	39	$-0.53^{+0.23}_{-0.23}$	$-1.83^{+0.08}_{-0.09}$	19^{+4}_{-4}	135^{+24}_{-24}	$-3.5^{+0.5}_{-0.5}$	2606.6(2571.4)	$-0.55^{+0.23}_{-0.22}$	$-1.82^{+0.08}_{-0.11}$	$18.9^{+4}_{-3.4}$	119^{+29}_{-30}	$-3.5^{+0.5}_{-0.5}$	52^{+22}_{-22}	2597.9(2551.1)	8.7
39	41	$-0.29^{+0.3}_{-0.25}$	$-1.8^{+0.07}_{-0.15}$	$17.5^{+0.26}_{-0.26}$	99^{+26}_{-24}	$-3.2^{+0.5}_{-0.6}$	2557.7(2522.5)	$-0.23^{+0.3}_{-0.28}$	$-1.81^{+0.14}_{-0.13}$	$17.1^{+0.26}_{-0.26}$	84^{+24}_{-24}	$-3.2^{+0.5}_{-0.5}$	51^{+25}_{-24}	2547.1(2500.3)	10.6
41	43	$-1^{+0.5}_{-0.4}$	$-1.1^{+0.6}_{-0.4}$	9^{+5}_{-5}	66^{+8}_{-7}	$-2.44^{+0.08}_{-0.15}$	2578.5(2543.3)	$-1.1^{+0.5}_{-0.4}$	$-1^{+0.8}_{-0.6}$	7^{+4}_{-4}	65^{+11}_{-9}	$-3.4^{+0.4}_{-0.4}$	93^{+13}_{-11}	2563.5(2516.7)	15
43	45	$-0.4^{+0.4}_{-0.4}$	$-1.2^{+0.4}_{-0.4}$	9^{+5}_{-4}	38.9^{+3}_{-3}	$-2.31^{+0.18}_{-0.24}$	2511.5(2476.3)	$-0.48^{+0.35}_{-0.4}$	$-1.26^{+0.27}_{-0.27}$	13^{+6}_{-8}	$37^{+3.2}_{-3.1}$	$-2.67^{+0.21}_{-0.2}$	58^{+18}_{-19}	2504(2457.1)	7.5
45	50	$-0.4^{+0.5}_{-0.8}$	$-1.3^{+0.8}_{-0.5}$	$12.2^{+3.4}_{-4}$	49^{+7}_{-6}	$-2.47^{+0.16}_{-0.17}$	3520.4(3485.1)	$-0.3^{+0.28}_{-0.29}$	$-1.54^{+0.29}_{-0.28}$	$12.9^{+3.2}_{-4}$	44^{+5}_{-6}	$-2.53^{+0.19}_{-0.18}$	49^{+17}_{-18}	3512.7(3465.8)	7.7
50	70	$-0.2^{+0.5}_{-0.5}$	$-1.64^{+0.11}_{-0.27}$	$11.2^{+1.5}_{-1.8}$	51^{+8}_{-9}	$-2.66^{+0.28}_{-0.3}$	4977.5(4942.3)	$-0.1^{+0.5}_{-0.5}$	$-1.66^{+0.21}_{-0.19}$	$10.9^{+1.6}_{-2.4}$	43^{+6}_{-7}	$-2.64^{+0.25}_{-0.25}$	42^{+16}_{-17}	4968.1(4921.2)	9.4

TABLE 3
The calculated flux and derived parameters of GRB 211211A prompt emission.

t_1 (s)	t_2 (s)	$F_{\rm BB}$ (10^{-6} erg cm^{-2} s^{-1})	$F_{\rm obs}$ (10^{-6} erg cm^{-2} s^{-1})	$F_{\rm BB}/F_{\rm obs}$	$\Gamma_{\rm ph}$	$R_{\rm ph}$ (10^{10} cm)
0.5	1.5	$0.03^{+0.07}_{-0.02}$	$0.48^{+0.06}_{-0.06}$	$0.06^{+0.15}_{-0.05}$	$86.93^{+31.69}_{-20.19}$	$0.61^{+0.66}_{-0.42}$
1.5	2.5	$0.32^{+0.62}_{-0.28}$	$13.30^{+0.30}_{-0.20}$	$0.02^{+0.05}_{-0.02}$	$176.23^{+49.35}_{-31.14}$	$2.02^{+1.69}_{-1.07}$
2.5	3.5	$8.16^{+1.54}_{-1.66}$	$54.40^{+0.50}_{-0.40}$	$0.15^{+0.03}_{-0.03}$	$268.67^{+15.01}_{-15.22}$	$2.33^{+0.39}_{-0.40}$
3.5	4.5	$0.91^{+3.69}_{-0.85}$	$39.70^{+0.30}_{-0.70}$	$0.02^{+0.09}_{-0.02}$	$252.02^{+137.33}_{-58.45}$	$2.06^{+3.36}_{-1.43}$
4.5	5.5	$0.28^{+0.65}_{-0.25}$	$13.90^{+0.30}_{-0.10}$	$0.02^{+0.05}_{-0.02}$	$192.10^{+65.90}_{-40.46}$	$1.63^{+1.67}_{-1.03}$
5.5	6.5	$2.98^{+1.82}_{-1.99}$	$63.00^{+1.00}_{-0.30}$	$0.05^{+0.03}_{-0.03}$	$273.76^{+48.23}_{-49.10}$	$2.55^{+1.35}_{-1.37}$
6.5	7.5	$0.70^{+2.20}_{-0.66}$	$81.50^{+0.50}_{-0.50}$	$0.01^{+0.03}_{-0.01}$	$311.73^{+154.09}_{-100.38}$	$2.23^{+3.31}_{-2.16}$
7.5	8.5	$4.80^{+2.00}_{-2.10}$	$62.20^{+0.50}_{-0.40}$	$0.08^{+0.03}_{-0.03}$	$267.11^{+27.37}_{-27.73}$	$2.71^{+0.83}_{-0.84}$
8.5	9.5	$0.15^{+0.88}_{-0.14}$	$15.10^{+0.30}_{-0.20}$	$0.01^{+0.06}_{-0.01}$	$221.40^{+174.20}_{-73.68}$	$1.15^{+2.72}_{-1.15}$
9.5	10.5	$0.08^{+0.35}_{-0.07}$	$12.70^{+0.20}_{-0.20}$	$0.01^{+0.03}_{-0.01}$	$204.54^{+117.81}_{-54.60}$	$1.23^{+2.13}_{-0.99}$
10.5	11.5	$0.28^{+0.96}_{-0.27}$	$9.24^{+0.19}_{-0.17}$	$0.03^{+0.10}_{-0.03}$	$192.26^{+97.56}_{-58.06}$	$1.08^{+1.64}_{-0.98}$
11.5	12.5	$0.04^{+0.12}_{-0.03}$	$3.85^{+0.11}_{-0.10}$	$0.01^{+0.03}_{-0.01}$	$148.01^{+66.21}_{-37.63}$	$0.98^{+1.32}_{-0.75}$
12.5	13.5	$0.03^{+0.07}_{-0.02}$	$2.03^{+0.08}_{-0.08}$	$0.01^{+0.03}_{-0.01}$	$125.75^{+49.89}_{-28.54}$	$0.85^{+1.01}_{-0.58}$
13.5	15	$0.02^{+0.06}_{-0.02}$	$2.20^{+0.08}_{-0.06}$	$0.01^{+0.03}_{-0.01}$	$127.76^{+52.29}_{-30.06}$	$0.87^{+1.07}_{-0.62}$
15	17	$0.03^{+0.09}_{-0.03}$	$3.90^{+0.10}_{-0.04}$	$0.01^{+0.02}_{-0.01}$	$145.94^{+61.89}_{-36.96}$	$1.04^{+1.32}_{-0.79}$
17	19	$0.10^{+0.47}_{-0.09}$	$10.90^{+0.10}_{-0.20}$	$0.01^{+0.04}_{-0.01}$	$197.65^{+133.22}_{-63.08}$	$1.17^{+2.37}_{-1.12}$
19	21	$0.14^{+0.30}_{-0.12}$	$9.57^{+0.13}_{-0.14}$	$0.01^{+0.03}_{-0.01}$	$173.16^{+57.02}_{-37.15}$	$1.53^{+1.51}_{-0.98}$
21	23	$0.25^{+0.42}_{-0.22}$	$9.22^{+0.12}_{-0.13}$	$0.03^{+0.05}_{-0.02}$	$169.90^{+46.13}_{-34.54}$	$1.56^{+1.27}_{-0.95}$
23	25	$0.13^{+0.35}_{-0.12}$	$10.70^{+0.13}_{-0.17}$	$0.01^{+0.03}_{-0.01}$	$182.36^{+69.38}_{-38.22}$	$1.46^{+1.67}_{-0.92}$
25	27	$0.07^{+0.33}_{-0.06}$	$6.40^{+0.12}_{-0.12}$	$0.01^{+0.05}_{-0.01}$	$175.75^{+121.45}_{-59.16}$	$0.98^{+2.03}_{-0.99}$
27	29	$0.38^{+0.26}_{-0.31}$	$3.36^{+0.08}_{-0.08}$	$0.11^{+0.08}_{-0.09}$	$125.82^{+16.68}_{-17.90}$	$1.40^{+0.56}_{-0.60}$
29	31	$0.02^{+0.06}_{-0.02}$	$2.81^{+0.07}_{-0.06}$	$0.01^{+0.02}_{-0.01}$	$138.25^{+51.92}_{-29.94}$	$0.88^{+0.99}_{-0.57}$
31	33	$0.17^{+0.17}_{-0.15}$	$2.43^{+0.06}_{-0.07}$	$0.07^{+0.07}_{-0.06}$	$122.80^{+25.81}_{-24.50}$	$1.09^{+0.69}_{-0.65}$
33	35	$0.04^{+0.12}_{-0.03}$	$2.28^{+0.07}_{-0.08}$	$0.02^{+0.05}_{-0.02}$	$128.03^{+56.02}_{-30.89}$	$0.90^{+1.18}_{-0.65}$
35	37	$0.08^{+0.19}_{-0.07}$	$3.36^{+0.10}_{-0.08}$	$0.02^{+0.06}_{-0.02}$	$143.44^{+55.25}_{-37.13}$	$0.94^{+1.09}_{-0.73}$
37	39	$0.06^{+0.17}_{-0.05}$	$2.46^{+0.08}_{-0.08}$	$0.02^{+0.07}_{-0.02}$	$128.31^{+54.07}_{-30.66}$	$0.97^{+1.22}_{-0.69}$
39	41	$0.05^{+0.16}_{-0.04}$	$1.95^{+0.06}_{-0.07}$	$0.02^{+0.08}_{-0.02}$	$123.11^{+60.78}_{-33.25}$	$0.87^{+1.28}_{-0.70}$
41	43	$0.48^{+0.11}_{-0.14}$	$1.74^{+0.07}_{-0.07}$	$0.28^{+0.06}_{-0.08}$	$120.34^{+9.17}_{-9.59}$	$0.83^{+0.19}_{-0.20}$
43	45	$0.08^{+0.10}_{-0.07}$	$1.05^{+0.05}_{-0.04}$	$0.08^{+0.09}_{-0.06}$	$104.86^{+22.62}_{-19.58}$	$0.76^{+0.49}_{-0.42}$
45	50	$0.04^{+0.08}_{-0.03}$	$1.16^{+0.03}_{-0.04}$	$0.03^{+0.07}_{-0.03}$	$108.06^{+32.72}_{-22.00}$	$0.76^{+0.69}_{-0.47}$
50	70	$0.02^{+0.04}_{-0.01}$	$0.52^{+0.02}_{-0.02}$	$0.03^{+0.08}_{-0.02}$	$91.12^{+33.68}_{-18.95}$	$0.57^{+0.63}_{-0.36}$

TABLE 4
Derived parameters of GRB 211211A in a hybrid jet model.

t_1 (s)	t_2 (s)	$1+\sigma_0$	η	$R_{\rm ph}$ (10^{10} cm)	$\Gamma_{\rm ph}$	$1+\sigma_{\rm ph}$
0.5	1.5	11.57	26.46	0.51	71.17	4.31
1.5	2.5	21.71	38.16	1.54	131.05	6.34
2.5	3.5	4.18	97.49	2.59	291.33	1.40
3.5	4.5	28.45	57.89	1.41	167.94	9.83
4.5	5.5	31.82	42.32	1.09	125.05	10.79
5.5	6.5	12.63	73.34	2.17	227.15	4.09
6.5	7.5	82.86	57.57	1.15	156.42	30.56
7.5	8.5	7.31	79.44	2.68	256.82	2.27
8.5	9.5	87.35	45.45	0.56	105.38	37.76
9.5	10.5	122.25	36.58	0.56	91.13	49.18
10.5	11.5	27.43	51.29	0.71	123.36	11.43
11.5	12.5	76.10	28.70	0.51	75.17	29.12
12.5	13.5	59.24	25.84	0.47	68.10	22.53
13.5	15	73.64	24.71	0.46	65.66	27.77
15	17	89.47	26.48	0.53	71.80	33.07
17	19	91.10	38.27	0.58	94.59	36.94
19	21	42.91	34.85	0.95	105.14	14.25
21	23	22.60	39.56	1.15	121.69	7.36
23	25	54.28	35.86	0.85	103.18	18.91
25	27	80.90	35.89	0.49	85.97	33.85
27	29	4.65	40.46	1.57	137.02	1.38
29	31	94.71	25.78	0.43	66.13	37.00
31	33	8.88	36.59	1.01	110.63	2.94
33	35	42.08	28.19	0.55	75.94	15.66
35	37	32.97	34.42	0.61	89.68	12.68
37	39	29.91	30.00	0.65	83.59	10.76
39	41	30.64	29.34	0.57	79.06	11.40
41	43	2.63	54.13	1.00	141.83	···
43	45	9.28	33.40	0.67	91.03	3.41
45	50	21.26	28.19	0.55	76.05	7.90
50	70	24.26	24.05	0.39	61.14	9.56

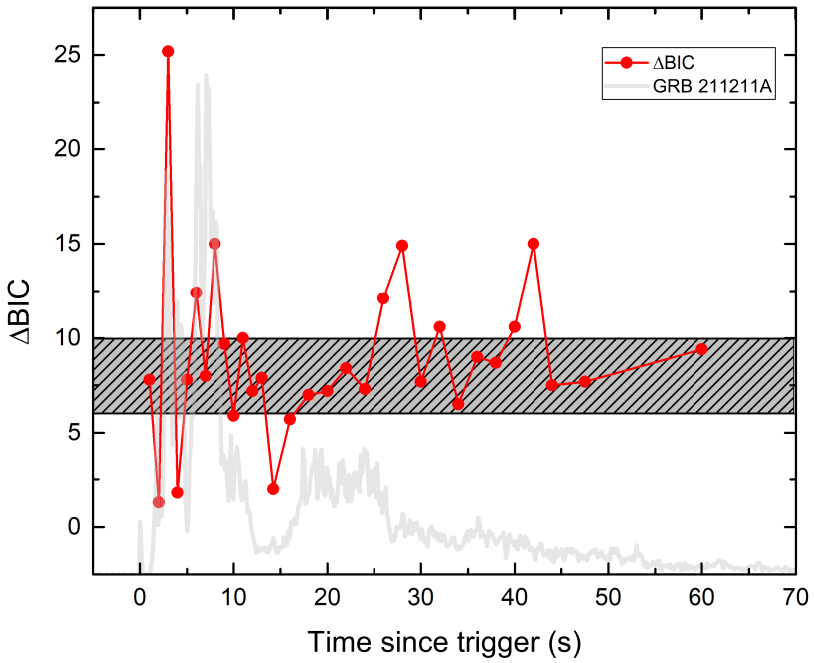


FIG. 1.— ΔBIC (solid red circles) between 2SBPL and 2SBPL+BB models in the time-resolved spectra of GRB 211211A. The gray line is the light curve of prompt emission, and the shaded area indicates the range of [6-10].

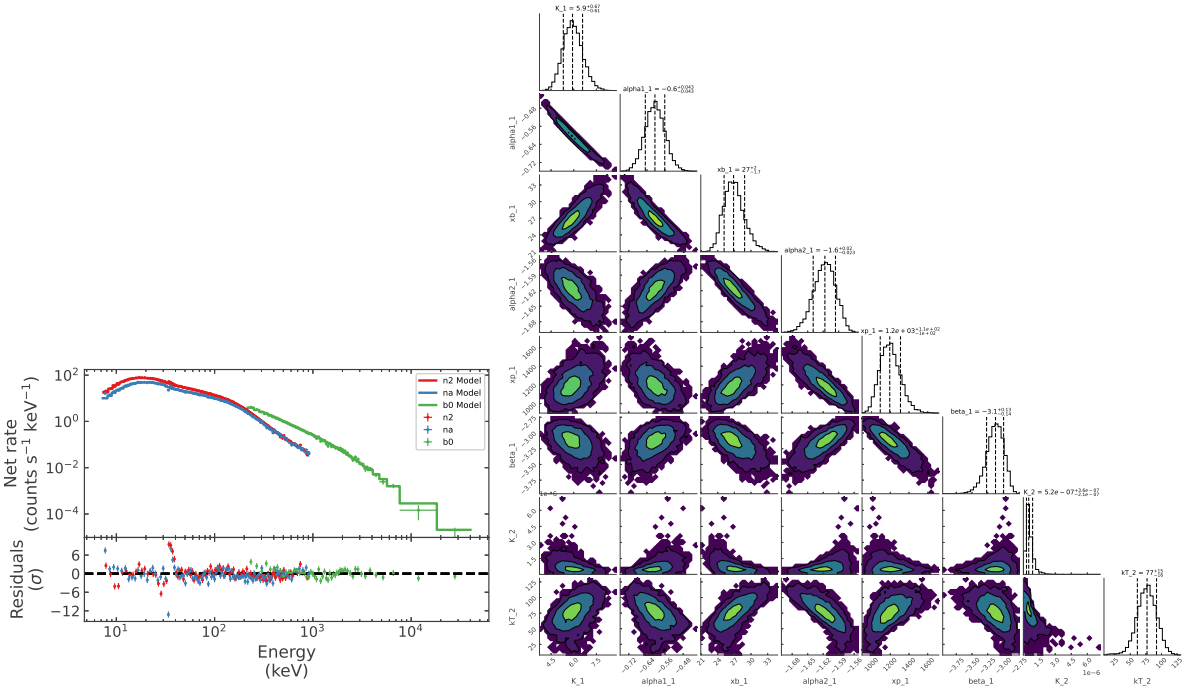


FIG. 2.— Time-integrated spectrum measured from $T_0 + 0.5$ to $T_0 + 70$ s is fitted by 2SBPL+BB model. Left: observed and modeled photon count spectra. Right: the parameter constraints of the spectral fit.

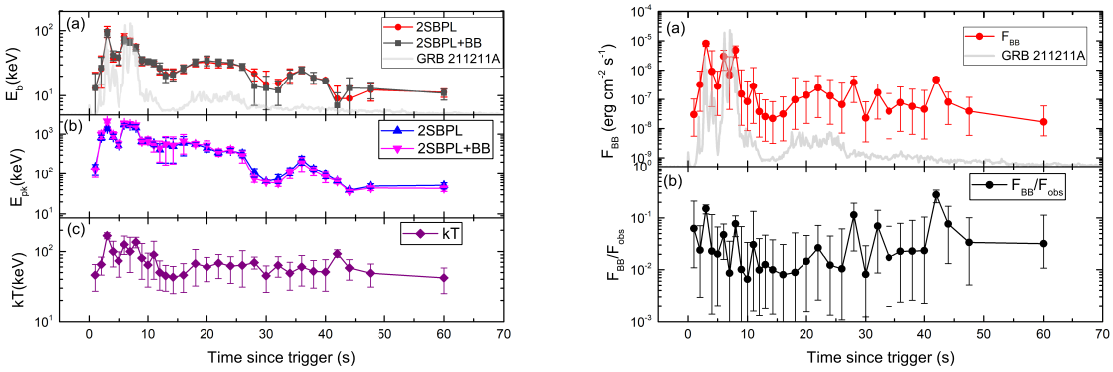


FIG. 3.— Left: temporal evolution of $E_{\rm b}$, $E_{\rm pk}$ and kT of 2SBPL+BB model. Right: similar to left panels, but for the flux ($F_{\rm BB}$) of BB emission and $F_{\rm BB}/F_{\rm obs}$.

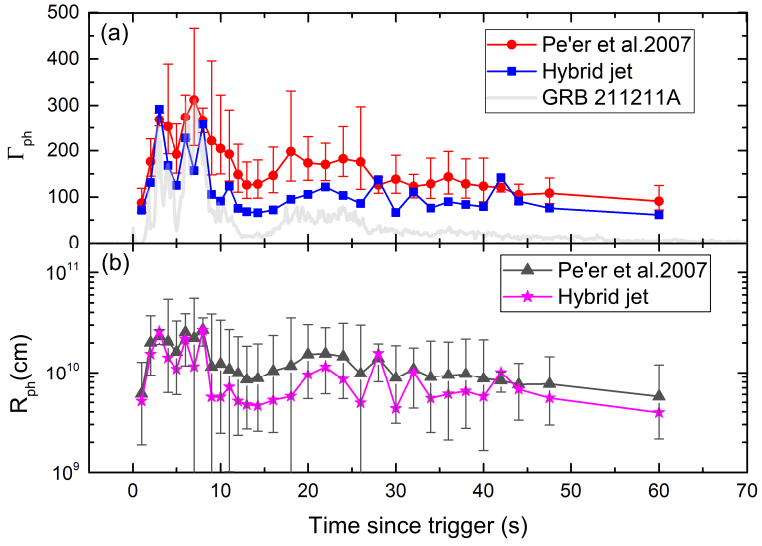


FIG. 4.— Temporal evolution of derived parameters $\Gamma_{\rm ph}$ and $R_{\rm ph}$ by using the Pe'er et al. (2007) model and hybrid jet (Gao & Zhang 2015).

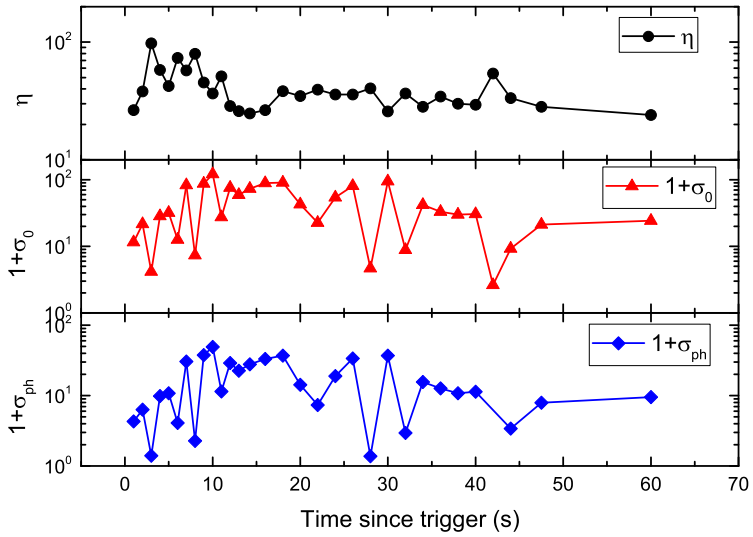


FIG. 5.— Temporal evolution of $1+\sigma_0$, η, and $1+\sigma_{\rm ph}$ in the hybrid jet model for fixed $r_0 = 10^7$ cm.

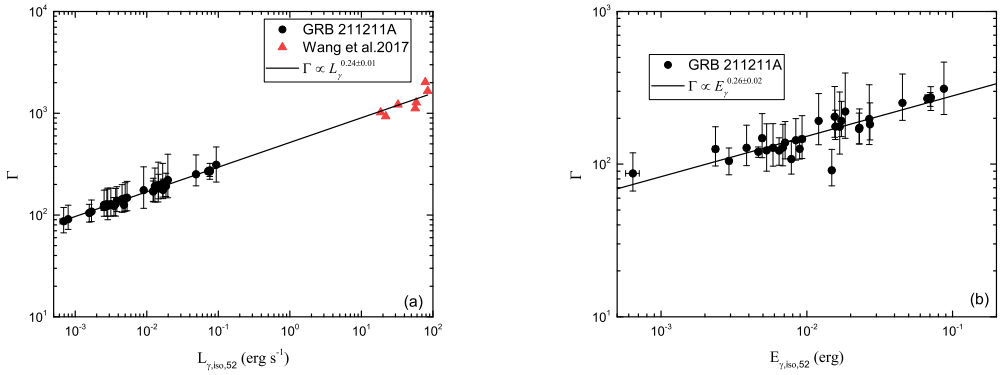


FIG. 6.— Lorentz Factor ($\Gamma_{\rm ph}$) as a function of $L_{\gamma,\rm iso}$ (a) and $E_{\gamma,\rm iso}$ of GRB 211211A (black solid circles). The black solid lines are the best fit with power-law model. The red triangles are the data of GRB 160625B from Wang et al. (2017).